Supplementary Information

Tailoring Dzyaloshinskii-Moriya interaction in a transition metal dichalcogenide by dual-intercalation

Guolin Zheng[#], Maoyuan Wang[#], Xiangde Zhu[#], Cheng Tan, Jie Wang, Sultan Albarakati, Nuriyah Aloufi, Meri Algarni, Lawrence Farrar, Min Wu, Yugui Yao, Mingliang Tian[*], Jianhui Zhou[*], Lan Wang[*]

# Those authors equally contribute to the paper.

* Corresponding authors. Correspondence and requests for materials should be addressed to J. Z. (email: jhzhou@hmfl.ac.cn); M. T. (email: tianml@hmfl.ac.cn); L. W. (email: lan.wang@rmit.edu.au).

1. Single Crystal Growth

Single crystals of $Fe_{1/3-\delta}TaS_2$ were grown via chemical vapor transport method with iodine as the transport agent. First, iron granular, Ta powder and sulfur sponges with mole ratio of 0.35:1:2 were mixed and sealed in an evacuated quartz tube. The tube was heated at 1173 K for one week. Second, the obtained powder together with about 120 mg iodine were sealed in an evacuated quartz tube with 15 mm inner diameter and 18 cm length. Then the tube was placed in a horizontal two-zone furnace, with source zone kept at 1223 K and growth zone kept at 1123 K for 10 days. The obtained as grown crystals were cleaned in ethanol with ultrasonic.

2. Device Fabrication and Transport Measurements

Solid protonic electrolyte was prepared by the sol-gel processes [1-3]. We first mixed tetraethyl orthosilicate (from Alfa Aesar), phosphoric acid (as a proton source, from Alfa Aesar, 85% wt%), ethanol and deionized water with a typical molar ratio 1:18:6:0.03, then the mixed solution was stirred for 2 hours and annealed for another 2 hours at 50 ℃ in a sealed bottle to form polymerized Si–O–Si chains. Finally, the substrate with bottom gate electrodes was spin-coated with the prepared protonic solution and baked at 150 ℃ for 25 mins.

$Fe_{1/3-\delta}TaS_2$ nanoplates were mechanically exfoliated from bulk crystals and placed on a silicon substrate with a 300 nm SiO_2 layer. Then the $Fe_{0.33-\delta}TaS_2$ nanoplates with suitable size and thickness were dry transferred by polydimethylsiloxane (PDMS) onto the protonic electrolyte (with thickness 300 nm). Both the exfoliation and transfer processes were carried out in a glove box full of high purity Argon gas with O_2 < 0.1 ppm, H_2O < 0.1 ppm. Hall-bar structures were fabricated by standard Electron-beam lithography (EBL) method followed by Cr/Au (10 nm/100nm) evaporation in a high vacuum sputtering system with base pressure less than

$5 \times 10^{-8}\, Torr$. Transport measurements were performed in a commercial Physical Property Measurement System (PPMS) with magnetic field up to 9 T. Protonic gating experiments were performed in commercial magnetic property measurement System (MPMS) with a maximal magnetic field of 7 T. To decrease the leaking current during the gating, voltage was swept at 250 K. Once the resistance was changed, the sample was quickly cooled down to low temperatures for magneto-transport measurements.

3. **Theoretical Calculations**

First-principles calculations are performed by using Vienna ab initio simulation package (VASP) [4, 5] based on the density function theory with Perdew-Burke-Ernzerhof (PBE) parametrization of generalized gradient approximation (GGA) [6]. The energy cutoff of the plane wave basis is set as 350 eV, and the Brillouin zone of $Fe_{1/3}TaS_2$ is sampled by 12 ×12 ×6 k mesh. The ionic positions are fully optimized until the force on each atom was less than 0.01 eV/Å while the lattice parameters are fixed as the experimental value. The intrinsic anomalous Hall conductivity [7] is calculated based on the Wannier90 code [8, 9] with s, d orbitals of Fe and Ta atoms and s and p orbitals of S atoms. The k mesh for intrinsic hall conductivity calculation is $100 \times 100 \times 50$ with an adaptive refinement mesh of size of $5 \times 5 \times 5$. Note that in the simulation of the impact of gating, we adopt the rigid band approximation and neglect the modification of band structures. The total energy calculation for DMI is based on GGA+U method [10, 11] with U values of 2.5eV and 4eV for d orbitals of Ta and Fe atoms. Note that in the simulation of the impact of gating, we adopt the rigid band approximation and neglect the modification of band structures.

4. **Temperature dependent out-of-plane magnetization and longitudinal resistance.**

Fig. S1 shows the temperature dependence of out-of-plane magnetization and longitudinal resistance of $Fe_{0.28}TaS_2$ single crystal. With a perpendicular magnetic field of 500 Oe, the out-of-plane magnetization shows a dramatic upturn around 85 K, indicating the Curie temperature $T_c = 85\ K$, as shown in Fig. S1(a). The temperature-dependent longitudinal resistance of $Fe_{0.28}TaS_2$ nanoflake also exhibits a resistance anomaly around 85 K, in line with the magnetization of single crystals. Both transport properties and out-of-plane magnetization are line with previous studies [12-14].

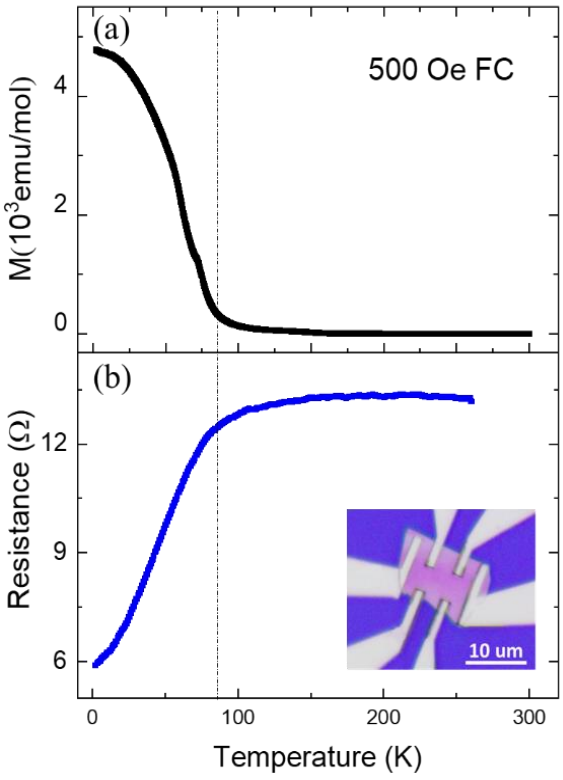

Figure S1. Temperature dependent magnetization and longitudinal resistance. (a) Temperature dependence of out-of-plane magnetization of $Fe_{0.28}TaS_2$ single crystal. (b) Shows the temperature dependence of longitudinal resistance in exfoliated nanoflake. Inset shows the optical image of a typical Hall-bar device (sample S3), with a thickness of 90 nm.

5. Square-shaped hysteresis loops above 20 K in sample S1.

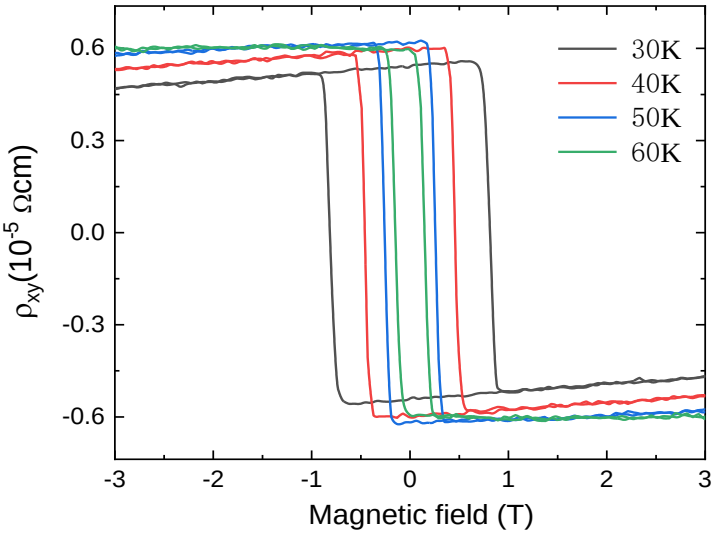

Figure S2. Hall resistivity above 20 K in sample S1. The hysteresis loops in sample S1 at selected temperatures (above 20 K) exhibit square-shaped loops with sharp transition near the coercive field.

6. Topological Hall effect (THE) observed in $Fe_{0.3}TaS_2$ single crystals.

As mentioned in main text, $\sqrt{3}a \times \sqrt{3}a$ type superlattice supports a sizable DMI and widely exists in Fe_xTaS_2 with different Fe doping concentrations. To verify this point, we further carried out the electric transport measurements in $Fe_{0.3}TaS_2$ crystals. Fig. S3 shows the transport properties of $Fe_{0.3}TaS_2$ single crystals at low temperature region. Akin to $Fe_{0.28}TaS_2$, the Hall resistivity exhibits extra humps (shadowed by light yellow), which are not proportional to the magnetization and should be attributed to THE due to sizable DMI. Note that the THE observed in $Fe_{0.3}TaS_2$ with a higher Fe concentrations emerges at low temperatures (within 4 K), compared with the THE in $Fe_{0.28}TaS_2$.

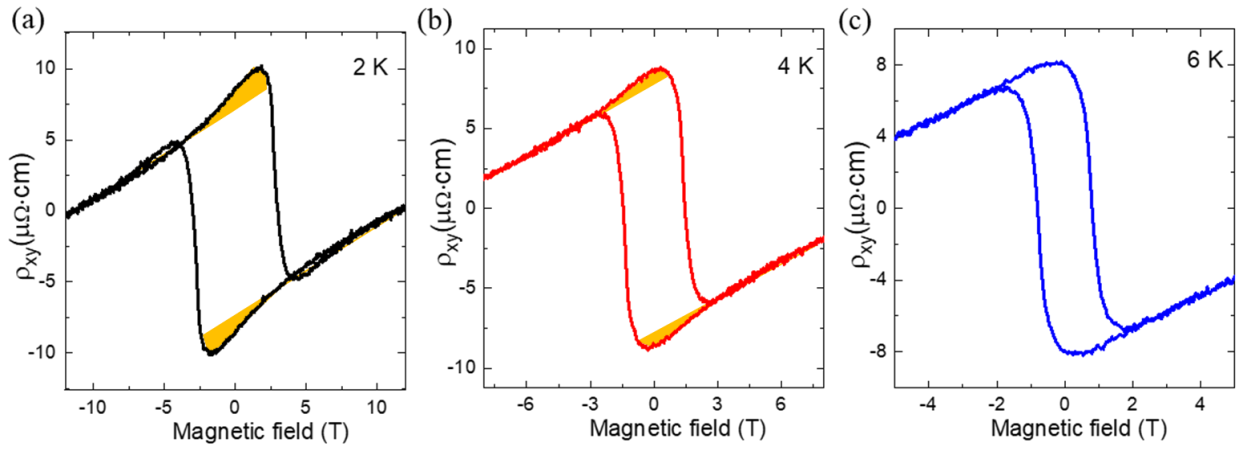

Figure S3. THE observed in $Fe_{0.3}TaS_2$ single crystals. The extra humps shadowed by light yellow are attributed to THE. The THE signal disappears after the temperature exceeds 6 K.

7. Longitudinal resistivity and anomalous Hall angle in $Fe_{0.28}TaS_2$ nanoflake (sample S1).

Fig. S4(a) exhibits temperature-dependent longitudinal resistivity in sample S1. The corresponding anomalous Hall resistivity and longitudinal magnetoresistivity at 3 K are shown in Fig. S4(b). The calculated anomalous Hall angle $\theta = \sigma_{xy}^{A}/\sigma_{xx} \sim 5\%$ ($\sigma_{xx} = \rho_{xx}/(\rho_{xx}^2 + \rho_{xy}^2)$, $\sigma_{xy}^{A} = \rho_{xy}^{A}/(\rho_{xx}^2 + {\rho_{xy}^{A}}^2)$). We also repeat the measurements in several samples and find that the anomalous Hall angle is $4.4\% \leq \theta \leq 5\%$. Such a large anomalous Hall angle in $Fe_{0.28}TaS_2$ is almost the same order as recently reported ferromagnetic semimetal Fe_3GeTe_2 [15], indicating a topological nontrivial origin.

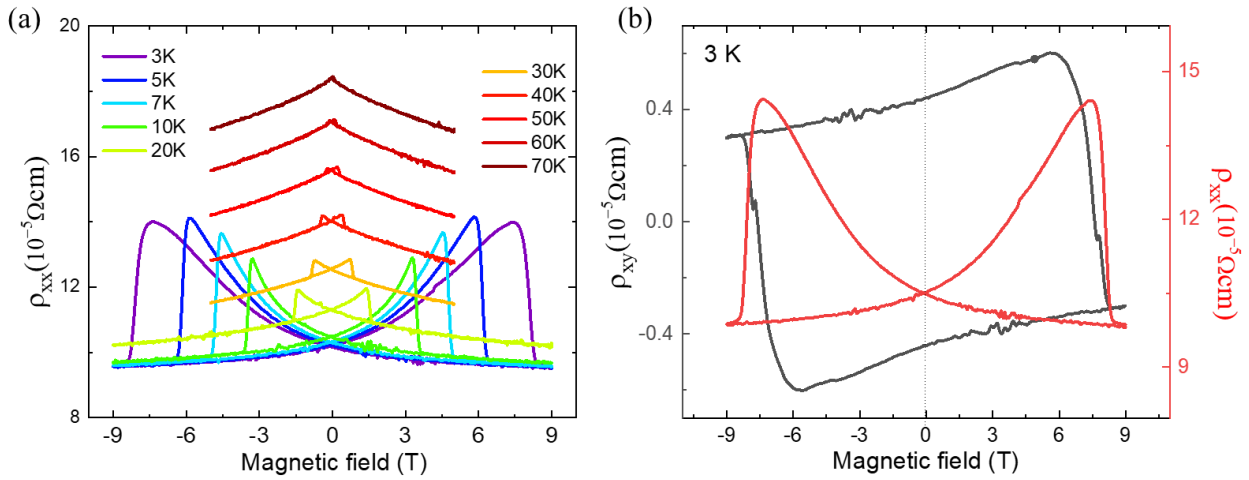

Figure S4. Large anomalous Hall angle in $Fe_{0.28}TaS_2$. (a) Temperature-dependent longitudinal magnetoresistivity. (b) Shows both Hall resistivity and longitudinal magnetoresistivity at 3 K. After subtracting the normal Hall resistivity ρ_{xy}^N, the anomalous Hall resistivity is given as $\rho_{xy}^A = \rho_{xy}(B = 0\ T)$.

8. Gate-dependent longitudinal resistivity and carrier density in sample S2 at 8 K.

Fig. S5(a) shows gate-dependent longitudinal resistivity in S2. Akin to gate-dependent anomalous Hall resistivities shown in Fig. 3b, the longitudinal resistivity can been dramatically enhanced when the gate voltages are swept from $V_g = 0\ V$ to $V_g = -5.2\ V$. Though the band structure is complex, the Hall resistivities between 4.5 T and 7 T are nearly linear with respect to magnetic fields. Analysing the Hall resistivity above coercivity field (as shown in Fig. S5(b)), we further found that the hole-type carrier density changed from $p = 9.05 \times 10^{22} cm^{-3}$ ($V_g = 0\ V$) to $p = 5.83 \times 10^{21} cm^{-3}$ ($V_g = -5.2\ V$). Such a dramatic modulation of carrier density in metallic magnet $Fe_{0.28}TaS_2$ reveals the ultra-high efficiency of protonic gate.

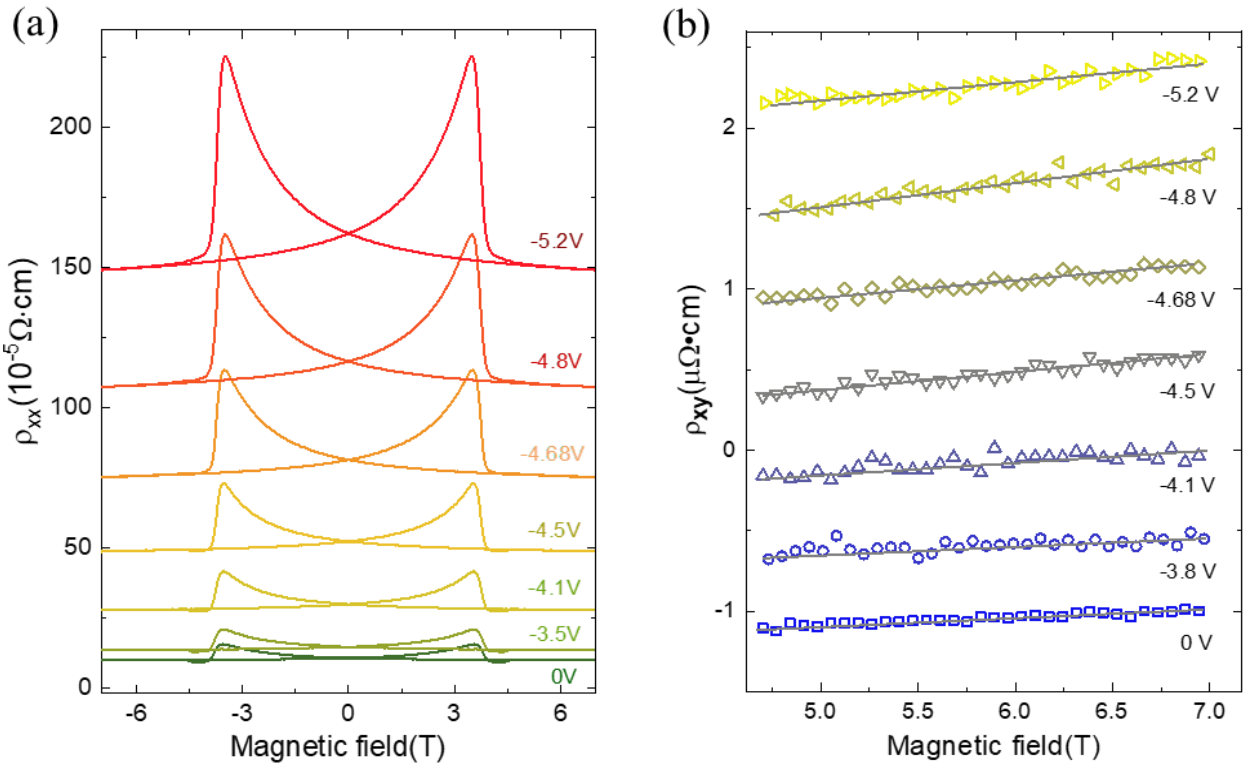

Figure S5. Gate-dependent longitudinal resistivity and carrier density in sample S2. (a) Gate-dependent longitudinal magnetoresistivity. (b) High field Hall resistivities under different gate voltages. Grey lines are linear fitting lines to experimental data under various gate voltages.

9. Density of states (DOS) of $Fe_{1/3}TaS_2$ near E_F=0 eV.

Figure S6 shows the calculated DOS of $Fe_{1/3}TaS_2$ near Fermi energy E_F=0 eV. The DOS around E_F=0 eV decreases when the E_F is shifted towards negative value. In the other hand, the AHC calculated in Fig. 2d declines while DMI in Fig. 4c increases accordingly. The gate-tuned both AHE and THE in Fig. 3b are well in line with our theoretical calculations. As the sweeping the gate voltages from 0 V to -5.2 V, the hole carrier density decreases gradually (Fig. S5(b)), while

the amplitudes of both anomalous Hall resistivity and topological Hall resistivity are elevated (AHC is decreased).

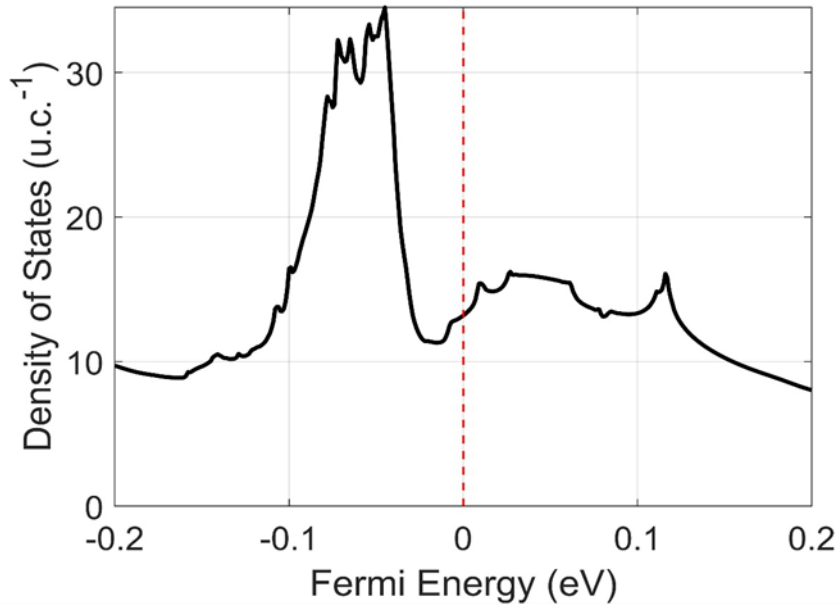

Figure. S6 Density of states (DOS) of $Fe_{1/3}TaS_2$ near E_F=0 eV. The DOS declines when E_F is shifted towards negative values.

10. Electron diffraction measurements

To characterize the $\sqrt{3}a \times \sqrt{3}a$ type superlattices of Fe_xTaS_2 with $0.28 \leq x \leq 0.33$, we take $Fe_{0.3}TaS_2$ single crystals as an example to carry out electron diffraction studies. Fig. S7 shows the selected area electron diffraction (SEAD) pattern. Besides the main structures (large bright spots, TaS_2 phase), we can see some superlattice reflections (faint, marked by red circle). This $\sqrt{3}a \times \sqrt{3}a$ type superlattices break the spatial inversion symmetry and support a sizable DMI, resulting in a large THE.

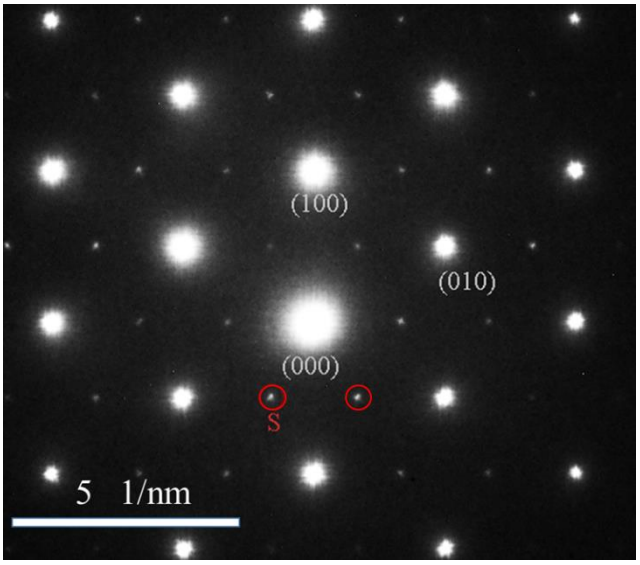

Figure S7. Electron diffraction pattern of $Fe_{0.3}TaS_2$. The reflections from superlattices are marked by the red circles.

11. Comparison of DMI between Bloch-type and Néel-type spin structures.

For a better understanding of the chiral spin structures in gate-tuned Fe_xTaS_2 nanoflakes, we also calculated the DMI in Néel-type spin structures. Fig. S8 shows the electron number N_e dependent DMI strength $d_\perp$($\propto \Delta_E^{DMI}$) for both Bloch-type and Néel-type spin structures. N_e=0 represents the case of E_F=*0*, and N_e=−1.5(+1) represents the Fermi energy around −80 meV(+50 meV). As we can see, the DMI of Bloch-type spin structures is larger than that of Néel-type spin structures. Besides, the DMI of Bloch-type spin structures in Fig. S8 highly depends on the Fermi energy, this is qualitatively consistent with our experimental observation in Fig. 3c (shifting the Fermi energy can largely increase the topological Hall resistivities). However, the DMI of Néel-type spin structures shows almost independent of the Fermi energy. Generally speaking, Néel-type

spin structures are usually observed in interface system or surface (ultra-thin film), while a Bloch-type spin structures are more likely to be observed in chiral bulk magnets. Thus, combining both theoretical analysis and experimental observations, we prefer a two-dimensional (2D) Bloch-type spin textures.

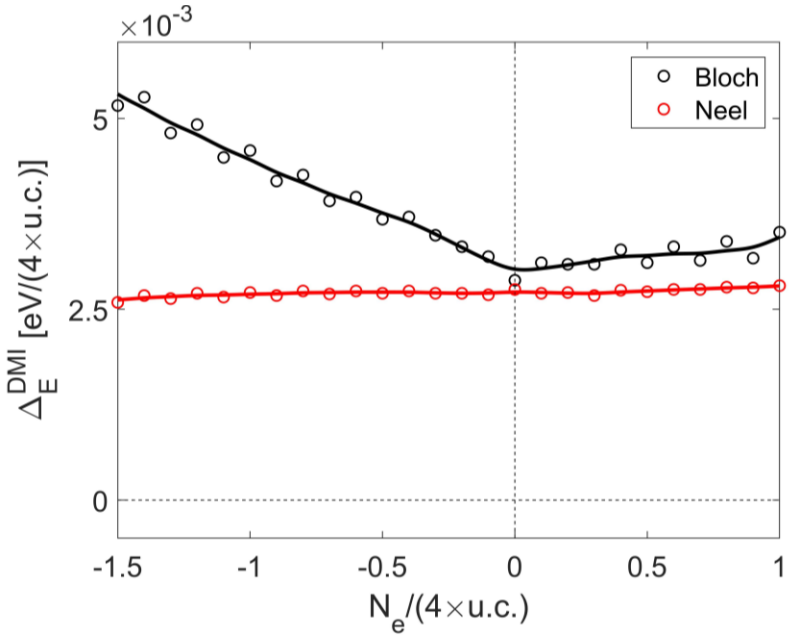

Figure S8. Comparison of DMI between Bloch-type and Néel-type spin structures. The electron number N_e dependent DMI strength $d_\perp$ ($\propto \Delta_E^{DMI}$) for both Bloch-type and Néel-type spin structures. N_e=0 represents the case of E_F=0, and N_e=−1.5(+1) represents the Fermi energy around −80 meV(+50 meV).

12. Comparison of THE to other compounds.

Table 1 shows the maximal magnitude of THE observed in different systems. The maximal amplitude of THE observed in van der Waals (vdW) magnet Fe_xTaS_2 reaches 1.4 $\mu\Omega \cdot cm$, the same order as recently observed giant THE in Frustrated triangular-lattice Gd_3PdSi_3 [22]. This

huge THE is larger than most of the known magnetic materials so far. The huge THE and anomalous Hall effect observed in our experiments indicates that vdW magnet Fe_xTaS_2 compound is a promising platform harbouring nontrivial spin textures associated with the Berry curvatures in both real and momentum spaces.

Table 1. The maximal THE observed in various compounds.

Compounds	Maximal THE ($\boldsymbol{\mu\Omega \cdot cm}$)	Notes	Refs
MnSi	0.0045	Chiral magnet	Ref. 16
Mn_5Si_3	0.05	Chiral magnet	Ref. 17
MnGe	0.16	Chiral magnet	Ref. 18
$SrRuO_3$ monolayer	~0.25	Correlated oxide	Ref.19
$Fe_{0.7}Co_{0.3}Si$	0.82	Chiral magnet	Ref. 20
$SrRuO_3$-$SrIrO_3$ interface	1.1	Interface system	Ref. 21
$Fe_{0.28}TaS_2$	1.4	Chiral vdW magnet	This work
Gd_3PdSi_3	~2.5	Frustrated triangular-lattice	Ref. 22
EuO	12	Centrosymmetric oxide	Ref. 23
$Ca_{0.99}Ce_{0.01}MnO_3$	120	Correlated oxide	Ref. 24

References

1. C. J. Brinker, G. W. Scherer, Sol-Gel science: The physics and chemistry of Sol-Gel Processing, (Academic Press, SanDiego, Califolia, USA, 1990).
2. A. H. Boonstera, J. M. E. Baken, Relation between the acidity and reactivity of a Teos, Ethanol and water mixture. *Journal of Non-Crystalline Solids* **122**, 171-182 (1990).
3. M. Jo *et al.*, Gate-induced massive and reversible phase transition of VO_2 channels using solid-State proton electrolytes. *Adv. Funct. Mater*. **28**, 1802003 (2018).
4. G. Kresse, J. Furthmuller, Efficient iterative schemes for ab initio total-energy calculations using a plane-wave basis set, *Phys. Rev. B* **54**, 11169 (1996).
5. G. Kresse, D. Joubert, From ultrasoft pseudopotentials to the projector augmented-wave method. *Phys. Rev. B* **59**, 1758 (1999).
6. J. P. Perdew, K. Burke, M. Ernzerhof, Generalized Gradient Approximation Made Simple. *Phys. Rev. Lett.* **77**, 3865 (1996).
7. Y. G. Yao *et al.*, First principles calculation of anomalous Hall conductivity in ferromagnetic bcc Fe. *Phys. Rev. Lett.* **92**, 037204 (2004).
8. A. A. Mostofi, J. R. Yates, Y.-S. Lee, I. Souza, D. Vanderbilt and N. Marzari, wannier90: A tool for obtaining maximally-localised Wannier functions. *Comput. Phys. Commun.* **178**, 685 (2008).
9. X. Wang, J. R. Yates, I. Souza, D. Vanderbilt, Ab initio calculation of the anomalous Hall conductivity by Wannier interpolation. *Phys. Rev. B* **74**, 195118 (2006).
10. V. I. Anisimov, J. Zaanen, O. K. Andersen, Band theory and Mott insulators: Hubbard U instead of Stoner I, *Phys. Rev. B* **44**, 943 (1991).
11. V. I. Anisimov, O. Gunnarsson, Density-functional calculation of effective Coulomb interactions in metals, *Phys. Rev. B* **43**, 7570 (1991).
12. Eibschütz, M. et al. Ferromagnetism in metallic Fe_xTaS_2 (x~0.28). *Appl. Phys. Lett.* **27**, 464 (1975).

13. Eibschütz, M. et al. Ferromagnetism in metallic intercalated compounds Fe_xTaS_2 ($0.20 < x < 0.34$). *J. Appl. Phys.* **52**, 2098 (1981).
14. Dijkstra, J., Zijlema, P. J., van Bruggen, C. F., Haas, C. & de Groot, R. A. Band-structure calculations of $Fe_{1/3}TaS_2$ and $Mn_{1/3}TaS_2$, and transport and magnetic properties of $Fe_{0.28}TaS_2$. *J. Phys.: Condens. Matter* **1**, 6363–6379 (1989).
15. Kim, K. et al. Large anomalous Hall current induced by topological nodal lines in a ferromagnetic van der Waals semimetal. Nat. Mat. 17, 794-799 (2018).
16. Neubauer, A. et al. Topological Hall Effect in the *A* Phase of MnSi. *Phys. Rev. Lett.* **102**, 186602 (2009).
17. Sürgers, C., Fischer, G., Winkel, P. & Löhneysen, H. v. Large topological Hall effect in the non-collinear phase of an antiferromagnet. *Nat. Commun.* **5**, 3400 (2014).
18. Kanazawa, N. et al. Large topological Hall effect in a short-period helimagnet MnGe. *Phys. Rev. Lett.* **106**, 156603 (2011).
19. Qin, Q. et al. Emergence of topological Hall effect in a $SrRuO_3$ single layer. *Adv. Mater.* **31**, 1807008 (2019).
20. Porter, N. A. et al. Giant topological Hall effect in strained $Fe_{0.7}Co_{0.3}Si$ epilayers. Preprint at https://arxiv.org/abs/1312.1722 (2013).
21. Matsuno, J. et al. Interface-driven topological Hall effect in $SrRuO_3$-$SrIrO_3$ bilayer. *Sci. Adv.* **2**, e1600304 (2016).
22. Kurumaji, T. et al. Skyrmion lattice with a giant topological Hall effect in a frustrated triangular-lattice magnet. *Science* **365**, 914–918 (2019).
23. Ohuchi, Y. et al. Topological Hall effect in thin films of the Heisenberg ferromagnet EuO. *Phys. Rev. B* **91**, 245115 (2015).
24. Vistoli, L. et al. Giant topological Hall effect in correlated oxide thin films. *Nat. Phys.* **15**, 67-72 (2019).